Comparative Evaluation of Three Coreholder Head Geometries on Axial and Radial Saturation Distributions Using CFD

Murilo Guimarães Morimoto[1*], *Nicolas* da Silva Riva[1], *Cláudia Míriam* Scheid, *Luís* Américo Calçada[1], *Cristiano* Agenor Oliveira de Araujo[1], *André Luiz* Martins Compan[2], *Luiz Augusto* da Cruz Meleiro[1], and *Filipe* Arantes Furtado[1].

[1]Laboratório de Escoamento de Fluidos Giulio Massarani (LEF), R. UJ UFRRJ, Seropédica, Rio de Janeiro – RJ, 23890-000, Brazil
[2]Petróleo Brasileiro S.A./Petrobras, Rio de Janeiro, Brazil

Abstract. This study employs computational fluid dynamics to evaluate how oil in a Buff Berea core can be displaced by brine when different coreholder heads are used. The Finite Volume Method (FVM) and commercial fluid dynamics software were used. The multiphase flow was simulated in the horizontal orientation and solved for various coreholder head layouts using the volume-of-fluid (VOF) numerical algorithm, which tracks the interface between phases. Moreover, relative permeability, capillary pressure, and gravitational effects were accounted for in the solution of the governing equations, thereby enabling a solid numerical approach. The homogeneity of the front flow was quantified using concepts from the variogram, a tool mainly used in geostatistical analysis. Findings indicate that, depending on the coreholder's head layout, a more homogeneous front flow can be achieved. The simulations show oil production varying by up to 32%, indicating that the core head layout may play a key role in assessing petrophysical properties. Based on the results, the use of head geometries that promote a uniform displacement front is recommended, as they improve sweeping efficiency.

1 Introduction

Energy consumption has increased over the past century. Therefore, studies that seek to improve oil extraction through petrophysics analysis are encouraged. To fully assess the reservoir's potential and recommend appropriate exploration techniques, it is crucial to understand the multiphase fluid dynamics within the reservoir and how measurement instruments can influence the scanning process. Hence, special petrophysics experiments conducted in coreholder devices are crucial for petroleum engineering.

A waterflooding experiment is a standard recovery process in which brine or freshwater is injected into a core plug to displace an organic phase. This technique is appropriate and commonly used by engineers to estimate key parameters, such as relative phase permeabilities and residual oil saturation [1]; hence, it improves the precision of operators' decisions regarding a reservoir's economic viability.

To obtain reliable information, it is essential that the shock front formed by brine injection uniformly sweeps the plug [1]. However, in a porous medium, one phase may naturally flow more readily than the other, leading to the formation of preferred flow paths known as viscous fingering [2]. This phenomenon may be facilitated by the large viscosity difference between oil and water, as well as by operational parameters and/or procedures, such as injection rate and incorporation of polymers into the injection stream [3,4].

It is suggested that the wavelength of viscous fingering in immiscible displacement could reach values greater than the core's dimensions, impairing the formation of multiple viscous fingers; hence, the influence of this structure would only be relevant in field-scale studies [5]. However, the development of multiple viscous fingers was experimentally and numerically observed in cores during standard waterflooding using immiscible fluids [6–9]. This mobility difference may cause water breakthrough to occur earlier, leading to an incorrect estimate of the field's recoverable oil.

To minimize the formation of possible viscous fingers, it is essential to supply the injection fluid to the core's face in the most homogeneously distributed manner possible, rather than concentrating it in a single zone of the rock's surface. This can be achieved by employing the inlet distributor piece, located upstream of the core plug, which is carved with grooves that better distribute the injection phase throughout the rock. The geometry of this component may alter the phase displacement within the core and influence the results. It is reported that, depending on the design of the end pieces, a radial flux can develop within the core as fluids converge towards these structures. Thus, favoring velocity instability in zones inside the core and near these end pieces [10]. Hence, studies investigating these structures and their influence on phase displacement are necessary. A simplified scheme of a waterflooding experiment and the coreholder (detailing its head and end pieces) is displayed in Figure 1.

* Corresponding author: morimoto@ufrrj.br

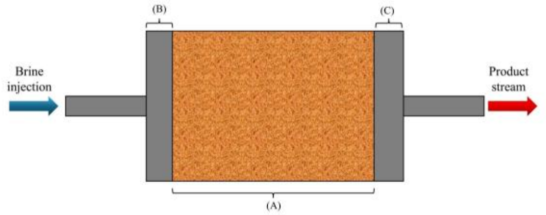

Component	Name
(A)	Core plug
(B)	Head piece / Inlet distributor
(C)	End piece

Fig. 1. Schematic of the waterflooding experiment and simplification of a coreholder device.

Parts of the coreholder that are in direct contact with saltwater are expected to be fabricated from costly, special-grade alloys based on chromium, nickel, and molybdenum, such as C276-alloy, to prevent oxidation-induced deterioration [11]. Within this framework, to avoid incurring the cost of constructing coreholders that yield no experimental gains, it is useful to employ Computational Fluid Dynamics (CFD) techniques to predict whether a geometric change to the device can enhance oil drainage by providing a more uniform front flow.

In a recent study, CFD simulations demonstrated the feasibility of assessing and comparing oil-gas sweep efficiency at the pore-scale domain when injecting miscible or immiscible CO_2 [12]. Moreover, CFD analysis enables determination of the relative permeability endpoint for each phase [13]. Nonetheless, breakthrough time, mobility control, and oil recovery factor can be well predicted using a correct numerical evaluation [14]. Lastly, the phase distribution within the core can also be visualized [16], which can help operators identify dead zones and how they might influence results. The numerical analysis of multiphase flow in porous media is a recurring topic in reservoir engineering. Yet, few studies investigate how the geometry and design of the coreholder may influence phase displacement.

Therefore, the main goals of this work are (i) to propose a reasonable numerical methodology to assess the oil-brine flow within a core plug and validate it using experimental data, and (ii) to evaluate the influence of the design of the coreholder's head and end pieces on responses such as pressure drop, oil residual saturation, and flow front homogeneity.

2 Numerical implementations

2.1 Governing equations and considerations

In this analysis, all relevant equations were solved using *ANSYS Fluent*®. The Volume of Fluid (VOF) multiphase model was selected to describe the transient flow of brine and oil throughout the core. This model is adequate when the interface position is of interest, as it can track the boundary between immiscible phases. Moreover, compared to other multiphase models, the VOF model is simpler; hence, it requires less computational effort, reducing simulation time. Furthermore, VOF is commonly used for multiphase flow in porous media [12,13] and has been applied in numerical studies in petrophysics [4,12,13,15]. In this research, it was assumed that no chemical species are transferred between phases and that no source or sink term exists in the continuity equation. Thus, the continuity for a "*q*" component is solved by Equation 1.

$$\frac{\partial\left(\alpha_q \rho_q\right)}{\partial t} + \nabla \cdot \left(\alpha_q \rho_q \mathbf{v}\right) = 0 \qquad (1),$$

where α_q and ρ_q are, respectively, the volume fraction and the density of phase q, and $\mathbf{v}$ is the phase velocity.

The velocity profile is obtained by solving the momentum equation (Equation 2). In this numerical evaluation, it is considered that the influence of the surface tension between the pair of phases can be assessed using the Continuum Surface Force (CSF) model proposed by Brackbill, Kothe, and Zemach [16], which is displayed as the third-to-last term of the right-hand side of Equation 2.

$$\frac{\partial\left(\rho \mathbf{v}\right)}{\partial t} + \nabla \cdot \left(\rho \mathbf{v}\mathbf{v}\right) = -\nabla P + \nabla \cdot \left[\mu\left(\nabla \mathbf{v} + \nabla \mathbf{v}^T\right)\right] + \\ + \rho \mathbf{g} + \sigma \frac{\rho \kappa \nabla \alpha_q}{0.5\left(\rho_q + \rho_r\right)} + \mathbf{S} + \mathbf{F_c} \qquad (2),$$

where ρ and μ are, respectively, the density and viscosity of the mixture. The pressure and gravity are defined, respectively, as P and $\mathbf{g}$. σ is the surface tension, which was considered constant. ρ_r is the density of phase *r,* and κ is the curvature of the interface. Lastly, **S** denotes the momentum sink due to the porous medium, and **Fc** accounts for volumetric capillary forces on the flow and is included in the momentum equation, as recommended by the *software* developer [17].

In this study, the computational domain does not describe the pores' microstructures. This strategy, commonly referred to as the Porous Media Model [17], is a widely used approach for numerically modeling permeable media [18,19]. In this case, the momentum equations for cells in the free-flow and porous zones differ; in the latter, the sinking terms are included to account for viscous losses due to the permeable material (**S**) and the influence of capillary pressure (**F**C). Moreover, it is important to note studies that emphasize the need to couple the porous and free-flow zones with a condition to better describe the flow over a porous surface [20,21]. However, these coupling conditions were not accounted for in this study.

The sinking term (**S**) was modeled using Darcy's law and is described in Equation 3. A velocity boundary condition of 0.000321 m/s was applied at the 2.60 mm diameter inlet port of the coreholder, corresponding to the injection of pure brine at a flow rate of 1cm³/min. At the other end, a pressure outlet boundary condition was chosen for the coreholder exit. Lastly, the capillary force interactions were modeled using the $\mathbf{F_c}$ and σ dependent terms, and no additional explicit correction was considered for capillary end effects.

$$S = -\frac{\mu}{K_{UDF,q}}\mathbf{v} \quad (3),$$

where K_{UDF} is the effective permeability of a generic phase "q". The UDF subscript stands for User-Defined Function, as described below.

In a porous medium, one phase can hinder the movement of another; therefore, the true permeability experienced by one phase is not equal to the absolute permeability of the medium. This must be accounted for in the modeling to better represent the physical flow within the core and is included in the effective permeability term (K_{UDF}) of Equation 3. To calculate this term, the relative permeability concept was applied using the Corey model, which was incorporated into the solution as a User-Defined Function (UDF). Equations 4 and 5 are, respectively, the relative permeability for the wetting phase (brine) ($K_{r,W}$) and for the non-wetting phase (oil) ($K_{r,O}$). Lastly, the normalized brine saturation ($\bar{S}$) used in the Corey model is shown in Equation 6.

$$K_{r,W} = K_{W,o}\left(\bar{S}^{N_W}\right) \quad (4),$$

$$K_{r,O} = K_{O,o}\left(1-\bar{S}^{N_O}\right) \quad (5),$$

$$\bar{S} = \frac{S_W - S_{WI}}{1 - S_{WI} - S_{OR}} \quad (6),$$

where $K_{W,o}$ is the relative permeability of brine at the irreducible water saturation (S_{WI}). $K_{O,o}$ is the relative permeability of oil at the residual oil saturation (S_{OR}). S_{NW} and S_{NO} are, respectively, fitting parameters.

For a given direction, the capillary influence may be accounted for in the momentum equation as the negative of the capillary pressure gradient in said direction [22]. In this research, aiming for the model's simplification and computational time gain, the gradient of the capillary pressure was considered numerically approximate to the ratio between the capillary pressure (implemented using the Brooks-Corey Model [23]) and a characteristic dimension, which, for this kind of flow, can be defined as the square root of absolute permeability [24,25]. This estimation is presented in Equation 7.

$$\mathbf{F}_C = -\nabla P_C \approx -\frac{P_C}{\sqrt{k}} = \frac{P_e \bar{S}^{-\frac{1}{\lambda}}}{\sqrt{k}} \quad (7),$$

where P_C is the capillary pressure, k is the absolute permeability, and P_e and λ are parameters of the Brooks-Corey Model, which were assessed using the experimental data of Santos *et al.* (2021) [26].

In this study, the experimental data reported by Santos *et al.* (2021) [26] were used to assist the development of the numerical implementation. According to Santos *et al.* (2021) [26], for the analyzed core, the imbibition cycle is mainly governed by spontaneous imbibition. Furthermore, insufficient data were provided to reliably fit more sophisticated models, such as the Skjaeveland model [27]. Hence, it is important to highlight that the model proposed should be preferably used for situations analogous to the one herein studied, since the capillary pressure in the forced imbibition cycle should be better accounted for. These considerations corroborated the use of the Brooks-Corey model to describe capillary pressure, even though it is traditionally used in drainage scenarios [28].

2.2 Validation

The data from the experimental imbibition study by Santos *et al*. (2021) [28] (presented in Table 1) were used as a benchmark to validate the numerical methodology in this work. Validation was performed by comparing the numerical predictions with the experimental observations reported by Santos *et al.* (2021) [26].

Table 1. Experimental data of Santos *et al*. (2021) [26]. Their data was used for validation.

Parameter	Value
Core dimension	Length: 4.78 cm Diameter: 3.82 cm
Core porosity	0.225
Core absolute permeability	597 mD
Brine properties	Density: 1142 kg/m³ Viscosity: 1.48 cP
Oil properties	Density: 856 kg/m³ Viscosity: 23 cP

Although Santos *et al*. (2021)[26] did not explicitly provide phase-relative permeabilities according to the Corey model, it is possible to estimate the appropriate parameters by fitting their experimental data to the model using nonlinear least-squares methods. This estimation led to an irreducible water saturation of 0.2000 and a residual oil saturation of 0.2767. $K_{W,o}$ and $K_{O,o}$ of, respectively, 0.0700 and 0.8995. S^{NW} and S^{NO} of 2.63 and 1.34, in that order. This procedure was extended to determine the coefficients for modeling capillary pressure, yielding $P_e = 4100$ Pa and $\lambda = 2.66$. Santos *et al.* (2021) [26] observed that oil production stabilized within 1 hour at a pure brine injection rate of 1 cm³/min, and the pressure drop stabilized at approximately 26.61 kPa.

In this numerical study, the properties of the phases and details regarding the core's porosity and permeability were the same as those adopted by Santos *et al.* (2021)[26]. This ensured that the fluids and core used in this numerical work were well aligned with data from their coreflooding experiment. In this analysis, the core, head, and end pieces were filled with a mixture of 80% oil and 20% brine (corresponding to the irreducible water saturation in the core).

2.3 Spatial domain

2.3.1 Head and end piece designs

The main goal of this study is to evaluate how the homogeneity of the flow front of brine can be disturbed by the design of the coreholder's headpiece. For this inquiry, three pieces were proposed and named: Spiderweb, Waffle, and Triangular. Identical free-flow head geometries were positioned at both ends of the core; however, the inlet and outlet points were arranged in diametrically opposite regions of the end pieces. As a result, these ports were not vertically aligned. All simulations were conducted in three dimensions. Furthermore, all numerical analyses in this work assumed the core to be incompressible and isotropic (with constant absolute permeability and porosity).

The Spiderweb design is a common layout provided by several companies and manufacturers. Our modeling of the Spiderweb headpiece is based on the commercial header available from JBV and consists of 5 concentric rings connected by 8 channels that radiate from the geometry center. Meanwhile, in Waffle's design, inspired by Leas's (1948) prototype [29], several squares are formed by crossing the horizontal and vertical gutters. Lastly, the Triangular geometry is a conception of our study group; the conduits in this piece are connected so that the resulting lattice resembles various equilateral triangles. In this study, the groove depth for all pieces was set to 0.65 mm, which is the commercial depth for Spiderweb. Details of the pieces' dimensions are presented in Figures 2-4. In these figures, the inlet orifice is highlighted in a darker color, and it is evident that brine injection is not centered in the diffuser.

Brine is admitted through the inlet orifice and fills the headpiece following its channels, represented by the light gray paths. These regions allow brine to flow from the headpiece to the core. On the other hand, the white portions of Figures 2-4 are the contact areas between the core and the headpiece. In these regions, fluids cannot flow. Lastly, it was sought to create headpieces that present a similar contact area; hence, obtaining a similar flow of brine from the inlet diffuser to the core plug.

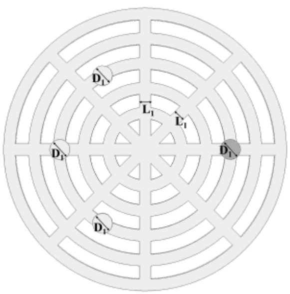

Dimension	Value (mm)
D_1	2.60
L_1	1.50

Fig. 2. Spiderweb head design.

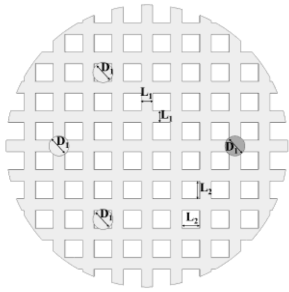

Dimension	Value (mm)
D_1	1.30
L_1	2.60
L_2	2.30

Fig. 3. Waffle head design.

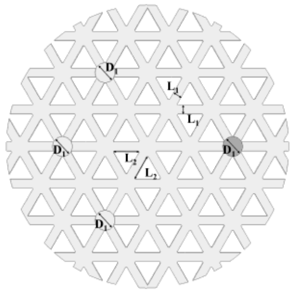

Dimension	Value (mm)
D_1	2.60
L_1	1.15
L_2	3.16

Fig. 4. Triangular head design.

2.3.2 Computational domain

The domain was spatially discretized in *ANSYS Software*. The core plugs analyzed measured 7.00 cm in length and 3.82 cm in diameter and were put in direct contact with the head and end pieces. Additionally, the computational coreholders presented the same geometry of the head and end pieces between the cores. As in the experimental setup of Santos *et al.* (2021) [26], the imbibition process was conducted in a horizontal configuration; hence, the gravity vector was perpendicular to the core. However, it is important to acknowledge that SCAL analyses are commonly performed in a vertical configuration. Therefore, the results presented in this study should be interpreted in the horizontal configuration and not extended to analysis conducted in the vertical orientation. In Figures 5 to 7, the spatial discretization of the three cores and the coreholder's heads studied is shown, with the inlet diffuser (free flow zone) in copper, the inlet port in blue, and the core (porous zone) in beige.

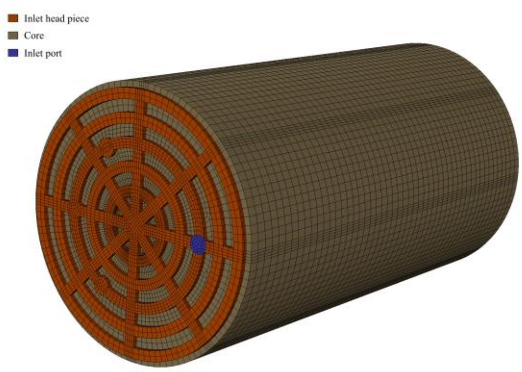

Fig. 5. Spiderweb computational mesh.

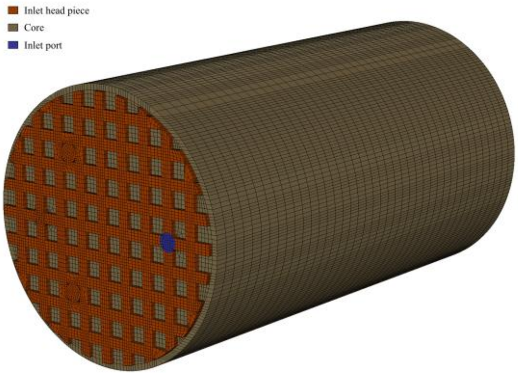

Fig. 6. Waffle computational mesh.

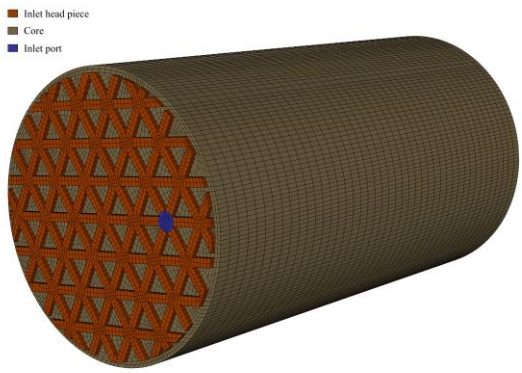

Fig. 7. Triangular computational mesh.

2.3.3 Mesh independence analysis

The procedure proposed by Celik *et al*. (2008) [30] was followed to ensure that the number of mesh elements did not affect the computational results. For this analysis, three meshes of the coreholder equipped with the Spiderweb head/end pieces were studied at low, medium, and high refinement. The low refinement mesh contained 76598 elements, while the medium and high refinement domains contained 180331 and 426215 elements, respectively.

Because the core volume is significantly greater than the volumes of the inlet and outlet head pieces, it was assumed that a mesh independence analysis could be performed using only one head piece geometry (Spiderweb). The number of cells in the mesh that ensures independence served as a reference for constructing the other grids. Hence, it was assumed that the computational domains of the other coreholders with a similar number of cells in the Spiderweb geometry also exhibited mesh-independent results.

2.4 Variogram

The variogram is a function employed in geostatistical studies to evaluate the difference in spatial variance between two points, thereby providing a measure of the spatial correlation of the observed parameter [19] and helping to assess its spatial dependence [31].

For a hypothetical cross section, parallel to the inlet face of the core, it is possible to couple the saturation of one phase to its spatial coordinates and evaluate how the saturation can change over a given distance. For a homogeneous flow, cell saturation in the cross-section is expected to be within a narrow range; hence, low variogram values are expected. On the other hand, high variogram values indicate uneven front flow because they indicate large differences in saturation across regions of a cross-section face.

Equation 8 displays a variogram that relates differences in variance to spatial distance. The points obtained with Equation 8 can be fitted into the exponential variogram model (Equation 9).

$$\gamma_{(h)} = \frac{1}{2}\frac{1}{N_{(h)}}\sum_{i=1}^{N_{(h)}}\left[\left(Z_{(xi)} - Z_{(xi+h)}\right)^2\right] \quad (8),$$

$$\gamma_{(h)} = C_0 + C\left(1 - e^{-\frac{h}{a}}\right) \quad (9),$$

where N is the number of pairs that are apart by a distance h from each other. $Z_{(xi)}$ and $Z_{(xi+h)}$ are, respectively, the variables for which we calculate the variogram. In this study, $Z_{(xi)}$ and $Z_{(xi+h)}$ are the saturation of oil in the cross-section of the core at position xi and at position h distant from xi, respectively. C_0 and C are the nugget point and an auxiliary parameter, respectively. Lastly, a is a distance parameter of the model.

The sill parameter (which is the sum of C_0 and C) is the key response of the variogram to evaluate the homogeneity of the front flow, because it can be concatenated to a situation where the difference between the saturations at a specified distance is high, pointing to the loss of homogeneity. In this study, the maximum difference between two points to be compared in the cross section was set as half of the core's radius, hence allowing a local analysis to track the face's homogeneity better.

3 Results and discussion

3.1 Validation and mesh independence

The validation study of the numerical approach was conducted in a core without any diffuser geometry (over the face of the entire core) until steady state was achieved, which was deemed attained when the difference in means over two consecutive 100 s flow time intervals for the oil remaining in the core was less than 0.05 cm^3. This analysis showed that the steady state was achieved within 5 hours of flow time, in good agreement with the observations of Santos *et al.* (2021) [26].

The oil residual saturation and the pressure drop reported by Santos *et al.* (2021) [26] were, respectively, 27.67% and 24.13 kPa. On the other hand, the numerical values obtained for the oil residual saturation and pressure drop were 26.08% and 19.61 kPa, respectively. Even though the coupling conditions between the free-flow and porous zones were not implemented as proposed in the literature [22,23], the numerical results were in good agreement with the experimental data. Hence, it is considered that the numerical approach and the considerations pondered are adequate and can represent this multiphase flow.

For the mesh independence analysis, the simulations were conducted using the coreholder equipped with the Spiderweb head and end pieces. Similarly, for the validation analysis, the independence study simulations were also conducted until steady state was judged to be achieved, which was within 1500 s of flow time. Table 2 presents the residual oil volumes and saturations obtained from the three analyses.

Table 2. Oil residual volumes and saturations within the core in the coreholder equipped with the Spiderweb head and end pieces.

Mesh refinement level	Residual oil volume (cm³)	Residual saturation
Low	9.20	0.5681
Medium	9.54	0.5891
High	9.47	0.5845

According to the proposed methodology, the results can be free of mesh size effects if the number of elements is approximately 180331; hence, a Medium degree of mesh refinement is required in this study. Therefore, the computational domain for all coreholders was constructed at this level. To summarize, the Spiderweb contained 180331 elements, while the Waffle and the Triangular contained 230048 and 194361 elements, respectively.

3.2 Numerical evaluation of the influence of head/end pieces design on the waterflooding

3.2.1 Filling pattern

The brine invasion through the headpieces is shown in Figure 8. For all studied geometries, brine occupied the inlet diffuser radially from the injection point. At steady state, more than 99% of the oil originally contained in the headpiece was displaced by water. The numerical assessment of the amount of oil exiting the inlet diffuser is crucial for accurately estimating the true volume of oil extracted from the core, thereby enabling a more precise assessment of the oil field's exploration potential. As brine is the denser phase, it first fills the bottom portion of the headpiece, indicating the influence of gravity in this free-flow zone.

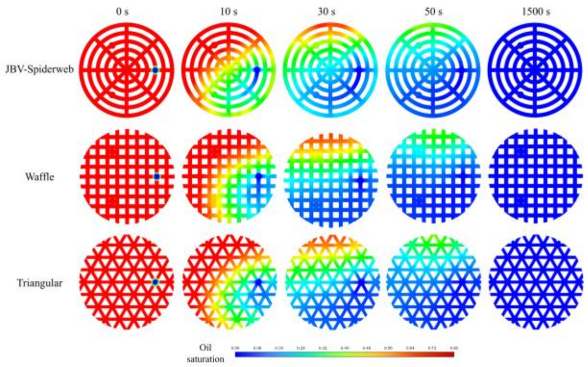

Fig. 8. Head diffusers filling pattern.

3.2.2 Advancement of the flow front

Figure 9 shows, for all coreholders studied, the steady-state brine penetration dynamics within a cross-section. It was observed that brine preferentially flows through the lower portions of the core, revealing the influence of gravity on the phase displacement within the porous region. However, it is worth mentioning that all simulations were conducted under the same conditions, which indicates that differences perceived may be linked to the design of the headpiece.

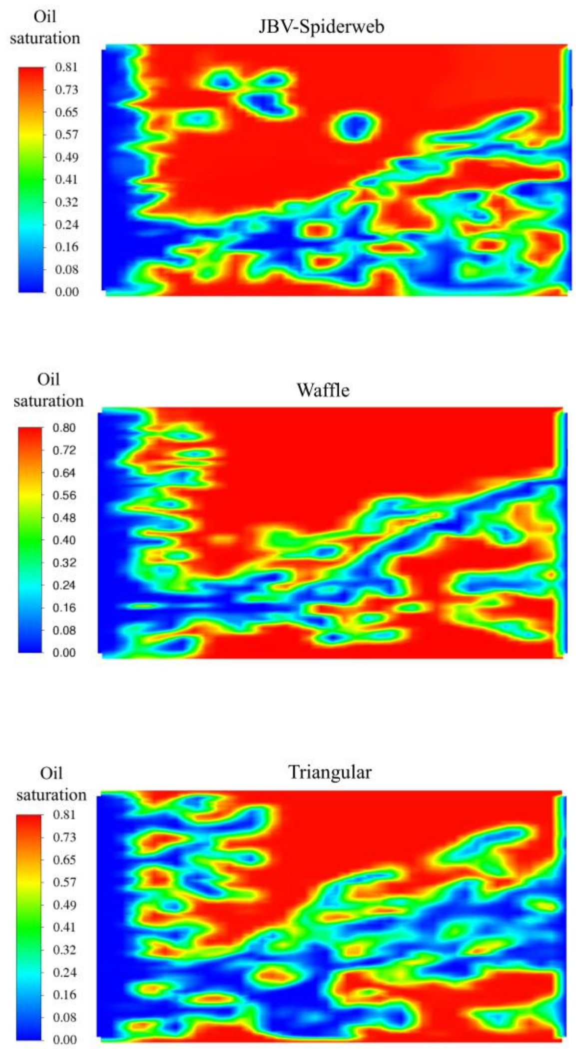

Fig. 9. Oil saturation in a cross-section of the coreholders studied.

It is observed that in the left portion of Figure 9 (near the inlet orifice) of the coreholder, the front flow of brine is remarkably homogeneous. However, the front flow becomes uneven, leading to formation of protuberances, which are not smooth and have branching behavior. A similar structural format was found in the experimental studies of Meurs *et al.* (1958) [32] and Sorbie *et al.* (2020) [33]. Additionally, this splitting was experimentally observed by Kargozarfard *et al.* (2019) [36], who used fluids with viscosities, densities, and interfacial tensions similar to those in this research. Therefore, the agreement between the simulated flow patterns and previously reported experimental observations suggests the physical validity of the numerical results.

While the injected brine is fed to the coreholder headpiece, it may begin penetrating the core before the shower piece is filled. This behavior favors the development of a preferential flow in the porous media beneath the injection point, leading to the formation of a dominant protuberance. Therefore, a zone of high water saturation forms, increasing the relative permeability of water and favoring the development of preferential flow. As the upstream platen fills, brine starts to penetrate the core through the other regions. As a result, the flow front remains relatively uniform in the core near the shower head. These results may indicate that the quantity of inlet points and their distribution on the head shower may play a role in controlling sweeping.

Furthermore, it can be observed that brine distribution becomes wider toward the outlet section of the core compared to the inlet portion. Because the outlet orifice is diametrically opposite to the injection point, the displacement front tends to converge progressively toward the outlet as it moves through the porous medium. Furthermore, this behavior may be enhanced by the growth of the protrusions of the dominant protuberance. Lastly, Figure 9 shows brine-rich zones in the middle of the core that are not connected to the dominant protuberance shown. As this displacement is a three-dimensional representation, these zones may be due to branching that are not analyzed in the cross-section shown. As these protuberances grow and ramify, they may transverse and intersect the analyzed plane.

According to Amrollahinasab *et al.* (2026) [5], for immiscible flows, the wavelength of viscous fingers may be in orders greater than the core, meaning that viscous fingers may not occur within the core. Therefore, the instabilities observed in this analysis may be due to the geometry of the headpiece. Therefore, the observed instabilities should not be confused with or categorized as viscous fingers. Moreover, it would be of great importance to conduct imaging studies to analyze the formation of such instabilities.

3.2.3 Core oil residual saturation and phase distribution

The residual oil saturation (S_{OR}) within the plug for the coreholders equipped with the Spiderweb, Waffle, and Triangular head/end geometry was 58.17%, 60.35%, and 54.25%, respectively. Thus, these results suggest higher overall oil production using the device equipped with the Triangular head geometry. Figure 10 shows the evolution of oil production as a function of the flow time. At steady state, reached at 1500 s, the oil produced with the Triangular geometry was nearly 4.63 cm³, while the amounts produced using the Spiderweb and Waffle were, respectively, 3.90 cm³ and 3.51 cm³. Hence, the Triangular geometry enhances the core's oil production by nearly 32% compared to the Waffle design.

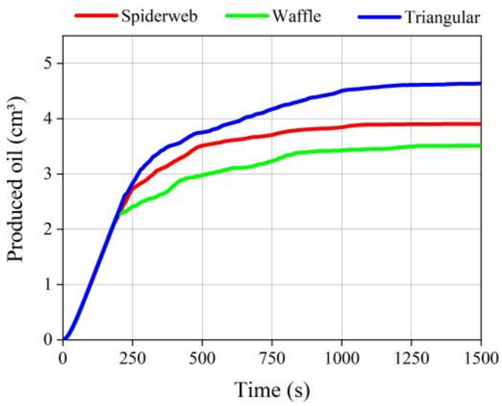

Fig. 10. Influence of head geometry on oil production.

Although the different inlet diffusers provide brine injection into the core over a similar area, the observed differences in S_{OR} values suggest that the head diffuser geometry plays a significant role in this fundamental response in coreflooding studies.

The different S_{OR} values obtained can be attributed to the sweep efficiency of the displacement flow. As shown in Figure 9, the coreholder with the Triangular inlet geometry promoted a more uniform sweep over a longer distance than the other geometries.

This fluid dynamic is also observed when analyzing the phase distribution at different cross sections of the core at steady state, as shown in Figures 11 to 13 for the coreholders equipped with the Spiderweb, Waffle, and Triangular head geometries, respectively. For all devices, an impression of the head geometry is readily seen in the cross sections near the interface between the inlet diffuser and the core, and fades as the front flow moves away from the core inlet.

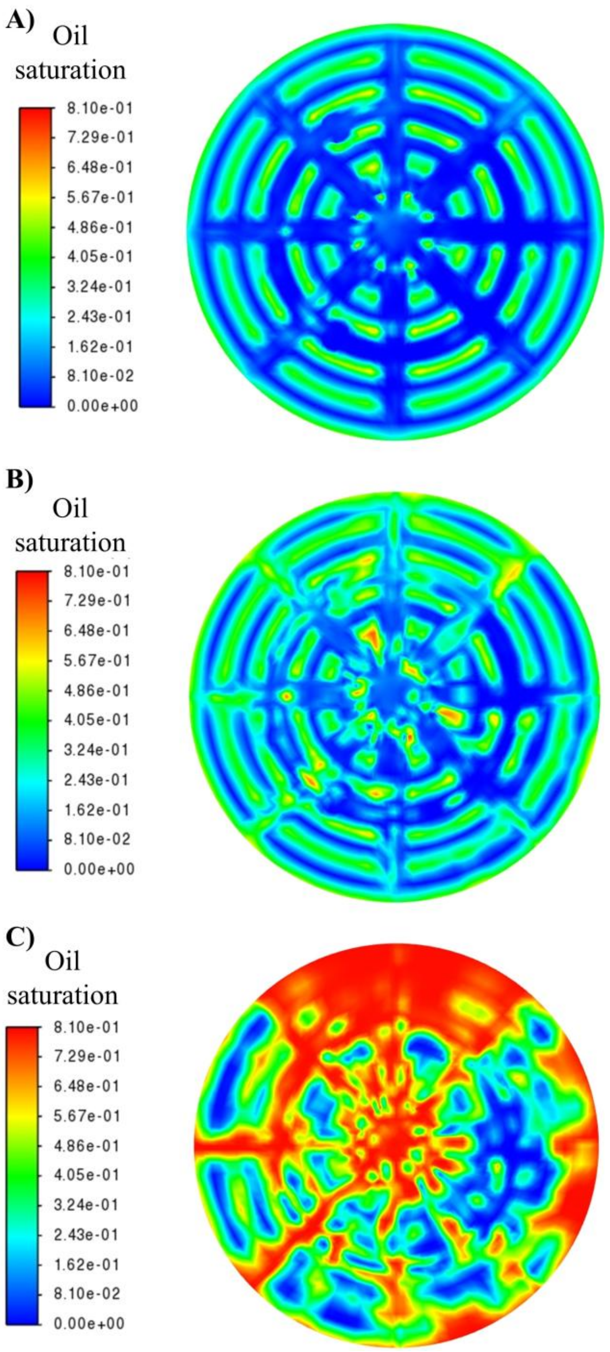

Fig. 11. Oil distribution in cross sections of the coreholder equipped with the Spiderweb geometry at distances of A) 3 mm, B) 5 mm, and C) 10 mm from the core's inlet after 1500 s of flow time.

Moreover, due to the gravitational force, oil would be expected to accumulate in the upper region, and brine would flow preferentially in the bottom portion of the core. This behavior is clearly seen in Figures 11 and 12 (for the Spiderweb and Waffle) and is less evident in the Triangular geometry (Figure 13). Hence, suggesting that the adverse gravitational effects in two-phase flow can be minimized, which could also explain the higher amount of oil produced when using this type of head geometry.

The superior performance of the triangular headpiece may be due to the connection pattern of its grooves. Unlike the other designs, the Triangular geometry has channels that are both horizontally and diagonally connected, which may have favored a more even distribution of brine at the interface between the core and the plug. Thereby, facilitating the sweep of brine in the core. Moreover, it is important to reinforce that as the results were influenced by the gravity the results herein obtained are valid for a horizontal configuration, results should not be extrapolated to coreholders in the vertical orientation.

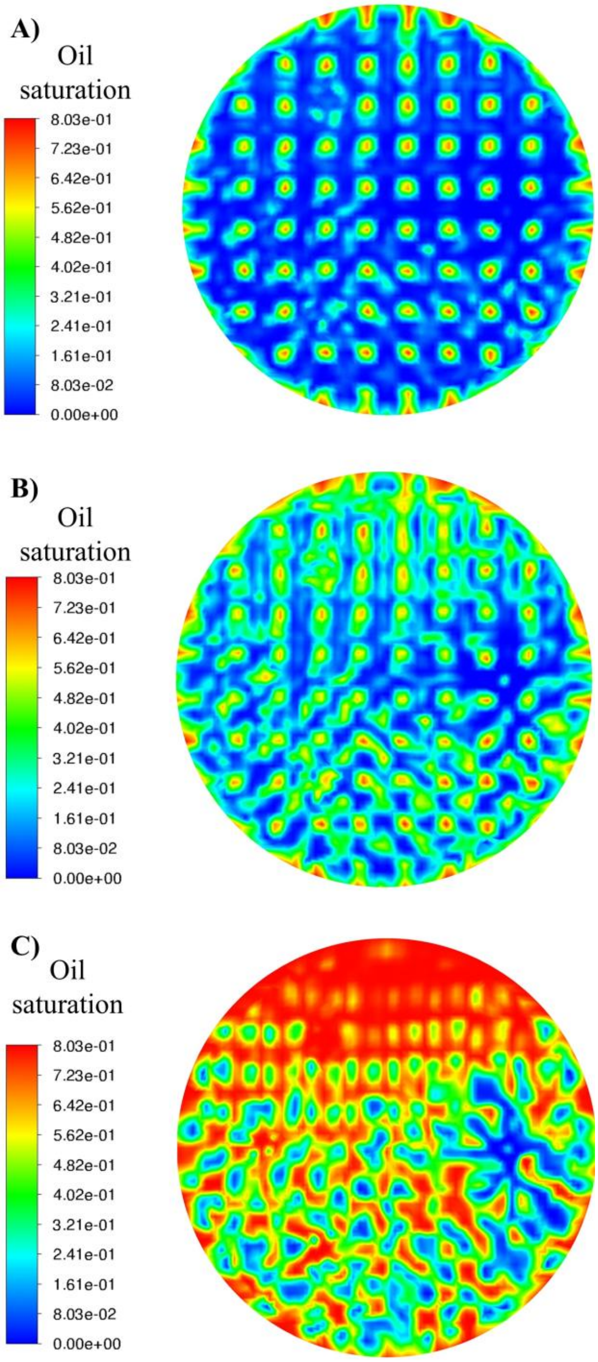

Fig. 12. Oil distribution in cross sections of the coreholder equipped with the Waffle geometry at distances of A) 3 mm, B) 5 mm, and C) 10 mm from the core's inlet after 1500 s of flow time.

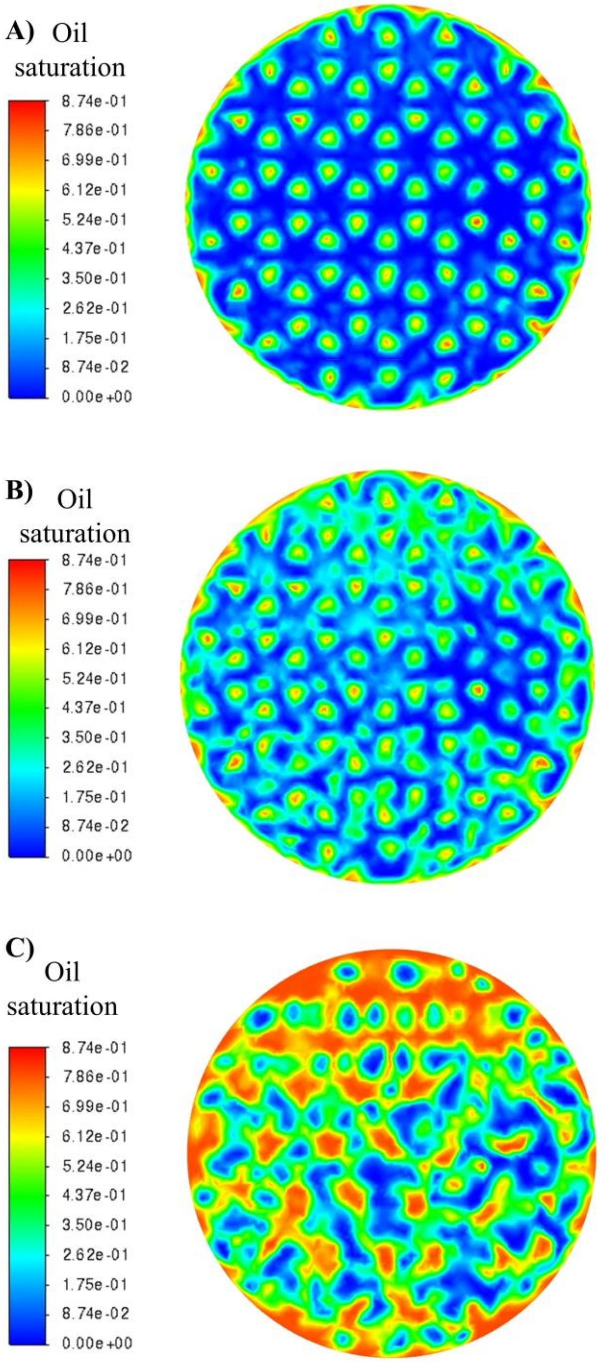

Fig. 13. Oil distribution in cross sections of the coreholder equipped with the Triangular geometry at distances of A) 3 mm, B) 5 mm, and C) 10 mm from the core's inlet after 1500 s of flow time.

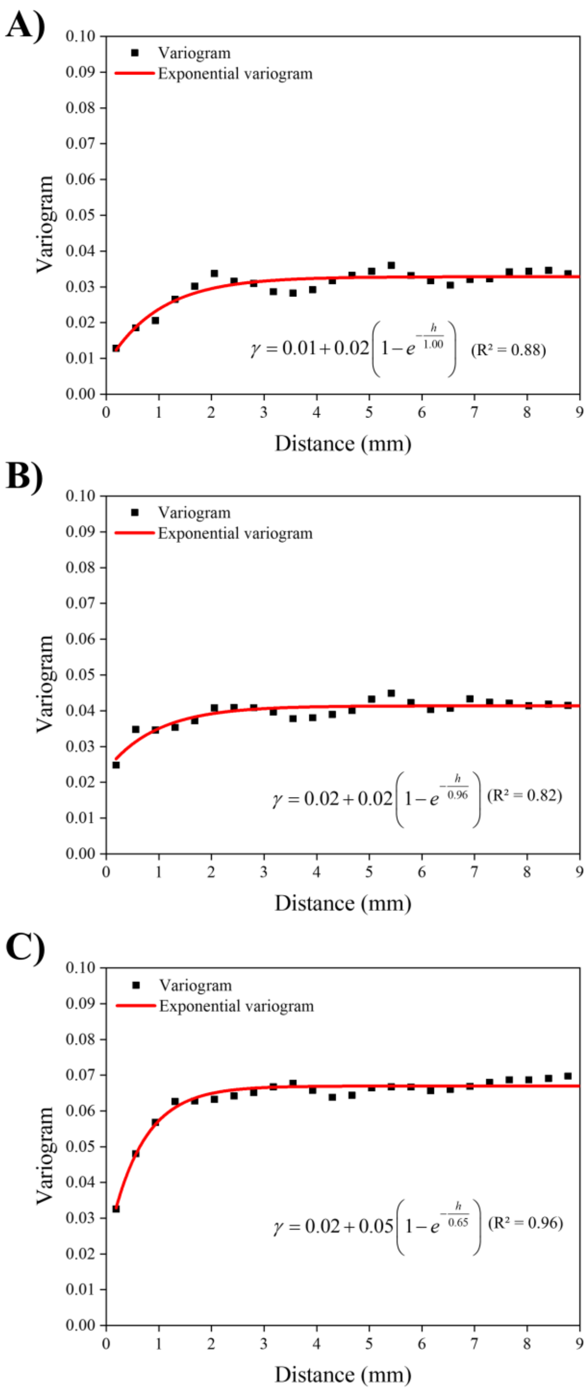

Fig. 14. Variogram of oil distribution at cross sections distant A) 1 mm, B) 5 mm, and C) 7 mm from the core's inlet for the coreholder equipped with the Spiderweb geometry after 1500 s of flow time.

3.2.3 Homogeneity limit of the injection flow

Results obtained at steady state (1500 s of flow time) were used to estimate the variogram, which was then used to determine the limit length beyond which the injection flow front is no longer considered homogeneous. The variogram for the coreholder equipped with Spiderweb head geometry at various cross-section distances from the core's inlet (1 mm, 5 mm, and 7 mm) is presented in Figure 14, along with the model fitting of the exponential variogram to the simulation data and its coefficient of determination (R^2).

Oscillatory behavior is observed in the plateau region of the variograms displayed in Figure 14. This phenomenon is caused by fluctuations in the distribution of phases across the core's cross sections due to the imprint of the head diffuser geometry, as shown in Figures 11 to 13. These oscillations reduce the coefficient of determination, resulting in values significantly below 0.99 for all fitted models.

The variogram values increase with distance to the comparison point, eventually reaching a plateau known as the sill. According to the variogram theory, for distances beyond which the sill is achieved, it is considered that the points compared exhibit little to no spatial dependence.

Moreover, it is observed that the sill value increases as the cross-section analysis becomes farther from the core's inlet, meaning an increase in the saturation oil gradient within the cross-section of the core, suggesting that the brine injection flow becomes less homogeneous.

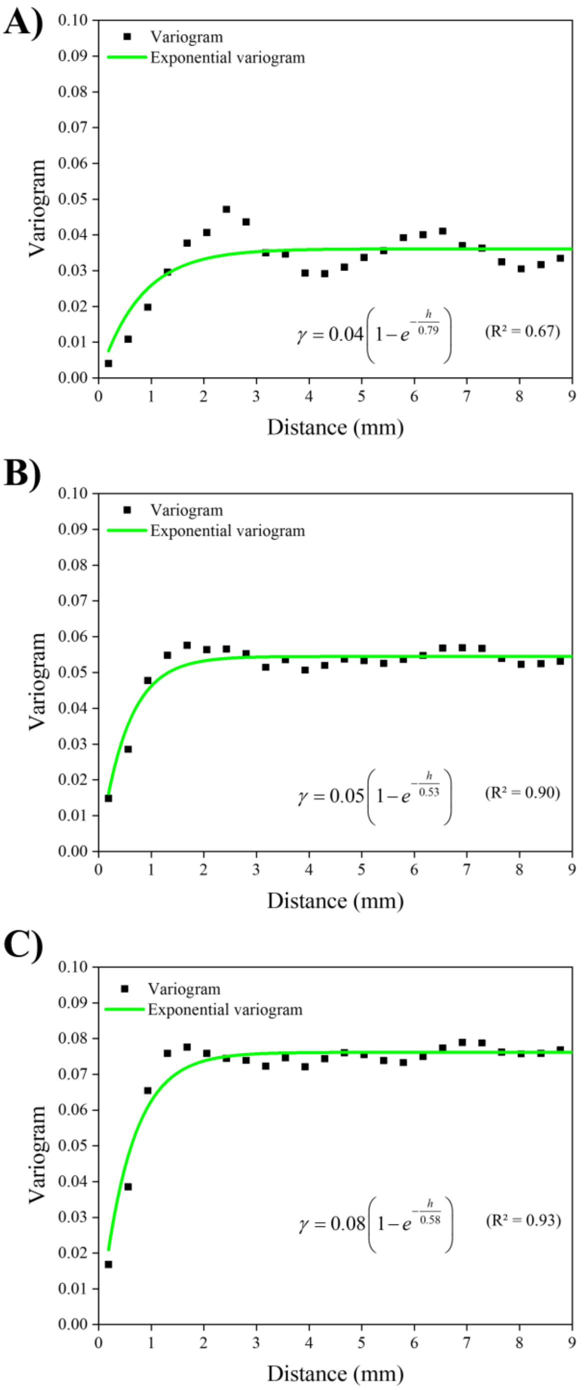

Fig. 15. Variogram of oil distribution at cross sections distant A) 1 mm, B) 5 mm, and C) 7 mm from the core's inlet for the coreholder equipped with the Waffle geometry.

Figures 15 and 16 present the variogram information for the coreholder equipped with Waffle and Triangular geometry, respectively. Comparing these two devices reveals the same variogram trend observed with the Spiderweb geometry; hence, the discussion of this geometry can be extended to the Waffle and Triangular devices.

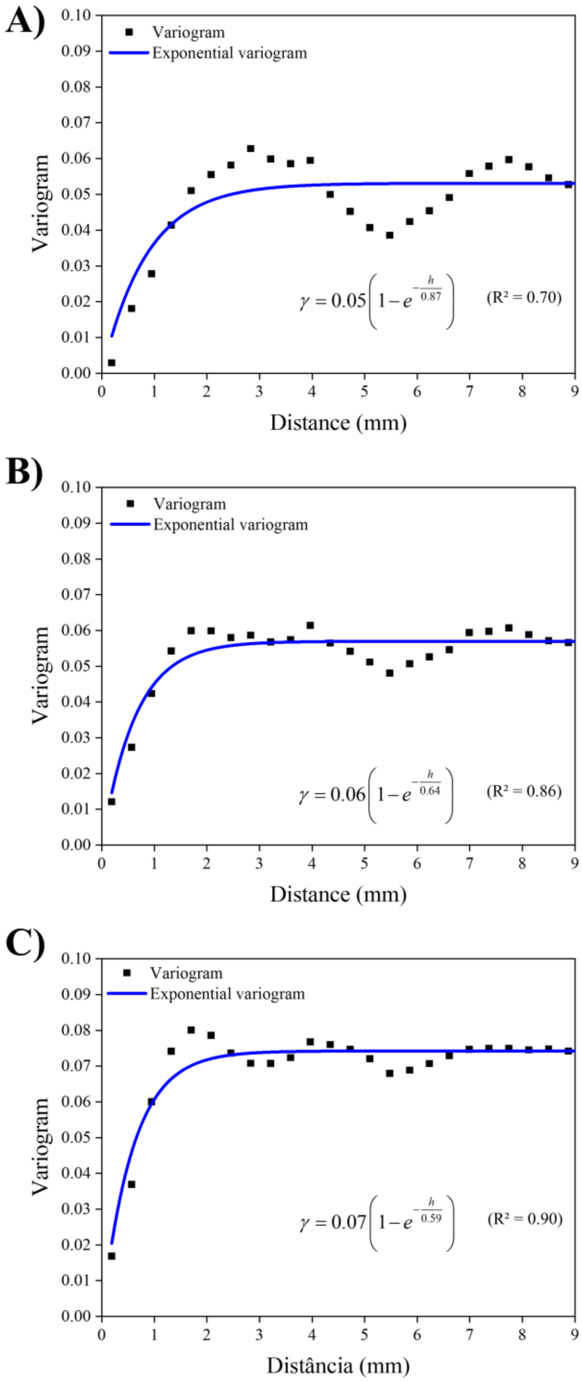

Fig. 16. Variogram of oil distribution at cross sections distant A) 1 mm, B) 5 mm, and C) 7 mm from the core's inlet for the coreholder equipped with the Triangular geometry.

In this study, the sill's value indicates the variance of saturation on a cross-section perpendicular to the flow direction. Low sill values indicate relatively uniform saturation within the analyzed cross-section, which could be associated with homogeneous front flow. However, high sill values indicate significant variation in saturation across the analyzed face, suggesting non-uniform flow. Therefore, the evolution of the sill value along the core length can serve as an indicator of flow stability, identifying the distance from the inlet at which the displacement front becomes non-uniform.

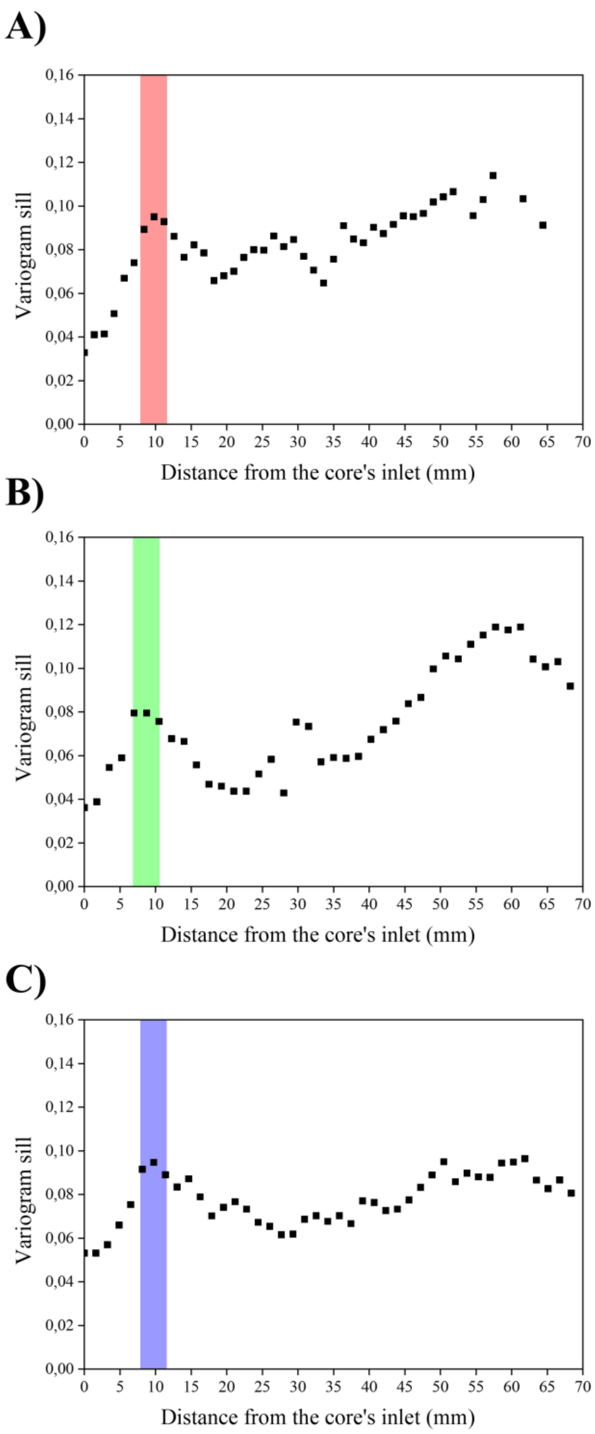

Fig. 17. Evolution of the variogram sill as the analyzed cross-section distances from the core's inlet for the of the coreholder equipped with the A) Spiderweb design, B) Waffle design, and C) Triangular design.

Figure 17 presents the evolution of the variogram sill as a function of distance from the core inlet for all coreholders equipped with the analyzed head piece geometries. The steep increase in the sill observed in Figures 14-16 becomes more evident in this analysis. However, it is shown that the sill reaches a maximum value and then it decreases. Considering a tolerance factor of ±5%, it is inferred that the front flow of the Spiderweb head diffuser loses its homogeneous behavior between 9.31 mm and 10.29 mm (9.80 mm on average) from the core inlet. For the Waffle geometry, the brine front becomes less homogeneous between 8.31 mm and 9.12 mm (8.72 mm on average) from the core inlet. Lastly, for the Triangular geometry, homogeneity is lost between 9.30 mm and 10.28 mm (9.79 mm on average).

4 Conclusion

Throughout this study, the influence of the coreholder headpiece geometry on flow-phase patterns in a porous medium was numerically analyzed. The numerical approach was able to represent multiphase flow within the core, as it reproduced a waterflooding experiment reported in the literature. Nevertheless, experiments using headpiece designs like those proposed in this study would be valuable for further assessing the model's predictive reliability. For a horizontal phase displacement, the results have shown that the geometry of the headpiece influences the homogeneity of the front flow, thereby affecting the fluid distribution within the plug and the amount of oil produced. Consequently, the headpiece design may influence oil recovery predictions and impact decisions related to reservoir management and its economic evaluation. Based on the results obtained, the Triangular design is recommended over the other geometries, as it provided a more uniform front flow, increasing oil production by nearly 32%. Furthermore, the variogram analysis proved an effective tool for identifying the distance beyond which the brine front flow is no longer considered homogeneous. However, it is important to reinforce and acknowledge that the flooding analysis in this study was performed in the horizontal configuration; therefore, the results obtained herein should not be extrapolated for coreholders in the vertical orientation. Lastly, it is important to note that the model for capillary pressure proposed in this study is limited for situations where imbibition is mainly driven by the spontaneous cycle.

Acknowledgments

The authors would like to thank PETROBRAS (Petróleo Brasileiro S.A.) for funding and support, as well as UFRRJ and the Fluid Flow Laboratory for its support in developing this work.

References

1. S. Berg and H. Ott, Int. J. Greenh. Gas Control **11**, 188 (2012).

2. X. Zhang, R. Wu, Y. He, J. Tang, J. Lu, and B. Wei, Colloids Surfaces A Physicochem. Eng. Asp. **734**, 139380 (2026).

3. A. Mansour, R. S. Al-Maamari, M. Souayeh, E. Artun, O. Al-Riyami, and A. Y. Al-Ghafri, Geoenergy Sci. Eng. **247**, 213725 (2025).

4. M. Norouzi, A. A. Yazdi, and A. K. Birjandi, J.

Nonnewton. Fluid Mech. **260**, 109 (2018).

5. O. Amrollahinasab, M. Abdellatif, H. Ott, and S. Berg, Phys. Fluids **38**, (2026).

6. A. Pinilla, L. Ramirez, M. Asuaje, and N. Ratkovich, Fuel **287**, (2021).

7. P. Singh and S. Mondal, Int. J. Multiph. Flow **184**, (2025).

8. S. K. Nandwani, N. Saxena, and A. Kumar, J. Mol. Liq. **396**, 124112 (2024).

9. D. I. E. N. Wijeratne and B. M. Halvorsen, Fuel **158**, 306 (2015).

10. S. Wang, X. Yu, W. Tang, C. Yu, and S. Wang, Energy Sources, Part A Recover. Util. Environ. Eff. **7036**, (2019).

11. S. Mohammadi, Heliyon **10**, (2024).

12. H. Xie, D. Liang, H. Peng, X. Wei, J. Zhao, J. Fu, and J. Zhang, Energy **334**, 137728 (2025).

13. T. Acharya, L. Song, E. Duginski, and A. Goodwin, Processes **11**, 1 (2023).

14. R. Gharibshahi, A. Jafari, A. Haghtalab, and M. S. Karambeigi, RSC Adv. **5**, 28938 (2015).

15. B. Hu, Z. Gu, C. Zhou, L. Wang, C. Huang, and J. Su, Appl. Sci. **12**, (2022).

16. J. U. Brackbill, D. B. Kothe, and C. Zemach, J. Comput. Phys. **100**, 335 (1992).

17. U. ANSYS Inc., **15317**, 724 (2012).

18. C. C. Wang and R. M. Wu, Sep. Purif. Technol. **198**, 60 (2018).

19. F. Garoosi, A. Kantzas, and M. Irani, Eng. Anal. Bound. Elem. **166**, (2024).

20. S. B. Gordon and D. J. Daniel, J. Fluid Mech. **30**, 197 (1967).

21. S. Ackermann, C. Bringedal, and R. Helmig, J. Comput. Phys. **429**, (2021).

22. P. Horgue, C. Soulaine, J. Franc, R. Guibert, and G. Debenest, Comput. Phys. Commun. **187**, 217 (2015).

23. J. Foroozesh and M. Jamiolahmady, Fuel **184**, 581 (2016).

24. G. S. Beavers, E. M. Sparrow, and D. E. Rodenz, J. Appl. Mech. Trans. ASME **40**, 655 (1973).

25. W. Zhong, X. Ji, C. Li, J. Fang, and F. Liu, Appl. Sci. **8**, (2018).

26. I. Santos, E. FM, N. DSS, C. J. CR, and P. Couto, Pet. Petrochemical Eng. J. **5**, (2021).

27. A. Kjosavik, J. K. Ringen, and S. M. Skjaeveland, SPE J. **7**, 49 (2002).

28. K. Li and R. N. Horne, Water Resour. Res. **42**, 1 (2006).

29. W. J. Leas, US Patent 2,618,151 (1948).

30. I. B. Celik, U. Ghia, P. J. Roache, C. J. Freitas, H. Coleman, and P. E. Raad, J. Fluids Eng. Trans. ASME **130**, 0780011 (2008).

31. J. Acosta, R. Vallejos, and P. García-Soidán, Spat. Stat. **69**, 100921 (2025).

32. P. van Meurs and C. van der Poel, Trans. AIME **213**, 103 (1958).

33. K. S. Sorbie, A. Y. Al Ghafri, A. Skauge, and E. J. Mackay, Transp. Porous Media **135**, 331 (2020).